

UAM: A Unified Attention-Mamba Backbone of Multimodal Framework for Tumor Cell Classification

Taixi Chen Jingyun Chen Nancy Guo*

State University of New York at Binghamton

Abstract

Cell-level radiomics features provide fine-grained insights into tumor phenotypes and have the potential to significantly enhance diagnostic accuracy on hematoxylin and eosin (H&E) images. By capturing micro-level morphological and intensity patterns, these features support more precise tumor identification and improve AI interpretability by highlighting diagnostically relevant cells for pathologist review. However, most existing studies focus on slide-level or patch-level tumor classification, leaving cell-level radiomics analysis largely unexplored. Moreover, there is currently no dedicated backbone specifically designed for radiomics data. Inspired by the recent success of the Mamba architecture in vision and language domains, we introduce a Unified Attention-Mamba (UAM) backbone for cell-level classification using radiomics features. Unlike previous hybrid approaches that integrate Attention and Mamba modules in fixed proportions, our unified design flexibly combines their capabilities within a single cohesive architecture, eliminating the need for manual ratio tuning and improving encode capability. We develop two UAM variants to comprehensively evaluate the benefits of this unified structure. Building on this backbone, we further propose a multimodal UAM framework that jointly performs cell-level classification and image segmentation. Experimental results demonstrate that UAM achieves state-of-the-art performance across both tasks on public benchmarks, surpassing leading image-based foundation models. It improves cell classification accuracy from 74% to 78% ($n=349,882$ cells), and tumor segmentation precision from 75% to 80% ($n=406$ patches). These findings highlight the effectiveness and promise of UAM as a unified and extensible multimodal foundation for radiomics-driven cancer diagnosis.

1. Introduction

Cell radiomics provides high-dimensional quantitative descriptors of tumor cell phenotypes, capturing attributes

such as size, shape, and high-order textural characteristics [9, 12, 16, 29]. These features translate abstract image semantics into objective, measurable representations that effectively characterize tumor phenotypes and their statistical properties, enabling more precise and interpretable diagnosis [12]. By directly highlighting diagnostically relevant cells for pathologist review, cell radiomics not only enhances diagnostic accuracy but also improves the interpretability of AI-assisted pathology.

Despite its promise, analyzing cell-level radiomics data remains a significant challenge. Most existing studies rely on slide-level or patch-level radiomics features for disease prediction and tumor identification [9, 14, 21, 31]. To enhance predictive precision, researchers have explored multimodal neural networks that fuse slide- or patch-level radiomics with features derived from Computed Tomography (CT), Magnetic Resonance Imaging (MRI), and H&E histopathology images [21, 31, 37], achieving accuracies between 64% and 77%. More recent work [9] demonstrated the effectiveness of Vision Transformers (ViT) [4] for analyzing radiomics features extracted from MRI, reaching up to 78% accuracy in predicting cognitive decline.

However, CT and MRI are limited to voxel-level representations and inherently lack cellular resolution. In contrast, H&E images provide thousands of pixel-level features per cell, offering a richer foundation for cellular-level analysis. Yet, this fine-grained modality, cell radiomics, remains largely unexplored. We hypothesize that (1) leveraging cell-level radiomics features enables more accurate tumor cell identification, and (2) integrating these features within a vision model can further improve tumor segmentation.

Nevertheless, there is currently no dedicated transformer backbone designed specifically for cell radiomics data. While ViT has been adapted for slide-level radiomics analysis [9], cell radiomics fundamentally differs from images: it constitutes a high-throughput sequence of structured features per cell rather than spatial pixel grids. Consequently, directly applying image-based backbones is suboptimal and likely to incur substantial precision loss.

To bridge these gaps, this work investigates two key as-

*Corresponding author: nguo1@binghamton.edu

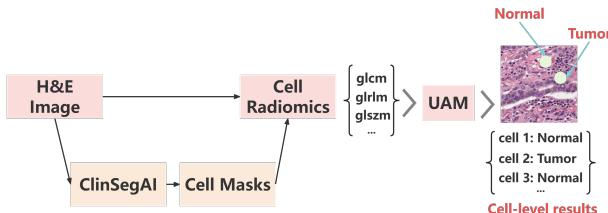


Figure 1. Overall pipeline. Using ClinSegAI, high-throughput cellular radiomics features are extracted directly from the source images. These features are then processed by the UAM model, which generates cell-level diagnostic predictions.

pects: (1) proposing a dedicated backbone optimized for cell radiomics analysis, and (2) constructing a multimodal architecture that fuses cell radiomics with visual information to enhance tumor diagnostic performance.

Accurate cell-level segmentation forms the foundation of the cell radiomics pipeline but remains a major bottleneck when performed manually by pathologists due to its labor-intensive nature. Recent advances in computer vision have alleviated this challenge by enabling automated generation of high-quality cell masks [3, 39]. For instance, ClinSegAI [3] introduces an image post-processing strategy that enhances BiomedParse [39] segmentation results and establishes a framework for extracting cell radiomics features to facilitate quantitative analysis, as shown in Figure 1. However, this work neither utilizes the extracted cell radiomics data directly for predictive modeling nor develops a dedicated backbone capable of effectively processing such data.

We approach the design of a cell radiomics backbone by examining the State-of-the-Art, the hybrid Attention-Mamba architecture, which has recently shown strong performance on radiomics-like sequential data. This architecture effectively combines the complementary strengths of Transformers [19, 33] and Mamba [6], achieving enhanced sequence modeling capability. Jamba [15, 30] is a representative implementation of this hybrid framework. However, its design enforces a fixed ratio between Transformer and Mamba layers, constraining architectural flexibility. Moreover, we observe that this structure tends to overfit when applied to cellular radiomics data (see Section 4 for detailed analysis). While MFuser[35] also adopts a hybrid configuration, it operates only as an adapter module and thus remains limited in representational capacity.

To address the lack of a dedicated backbone for cell radiomics data and to overcome the inherent limitations of existing architectures, we propose UAM, a *Unified Attention-Mamba* backbone, as shown in Figure 2. UAM introduces a highly flexible design that eliminates the need for manually tuning the ratio between Attention and Mamba layers, making it well-suited for analyzing cell radiomics datasets of varying sizes and feature dimensions. Specifically, the

UAM backbone is composed of two key components: the Amamba layer and the Amamba-MoE layer. The Amamba layer employs Mamba to generate context-enriched embeddings that capture long-term dependencies in linear time. These embeddings are then used as the *values* (V) in a cross-attention module, while the original input embeddings serve as the *queries* (Q) and *keys* (K). This design allows UAM to effectively interpret high-throughput radiomics sequences by seamlessly integrating Mamba-generated contextual information into the attention mechanism, enabling efficient and precise global information extraction. Building upon this, the Amamba-MoE layer concatenates the outputs from the Mamba and Attention branches, followed by a Mixture-of-Experts (MoE) module [5, 11, 27] to process the combined radiomics representations. Inspired by recent findings that MoE significantly enhances both Mamba and Transformer architectures [11, 15], this layer boosts UAM’s learning capacity and computational efficiency while maintaining strong generalization performance.

Extending this backbone, we further introduce a multimodal UAM framework for joint cell classification and image segmentation, as illustrated in Figure 3. This framework fuses radiomics embeddings from UAM with image embeddings from the BiomedParse encoder to produce more precise segmentation masks. Following the approach of LLaVA [17], we project radiomics embeddings into the image embedding space, enabling effective utilization of the pretrained BiomedParse decoder for downstream mask generation. Our contributions are summarized below:

- **Unified Backbone for Cell Radiomics:** We present the first dedicated backbone for cell radiomics analysis, UAM, a unified Attention-Mamba structure that flexibly models high-throughput, sequence-like cell radiomics.
- **Amamba Encoder:** We design the Amamba layer, which embeds Mamba-derived global contextual information into a cross-attention mechanism, enhancing global representation learning and model interpretability.
- **Amamba-MoE Encoder:** We propose the Amamba-MoE module that fuses Mamba and Attention outputs and applies a Mixture-of-Experts mechanism to further improve learning capacity and classification performance.
- **Multimodal Integration for Tumor Diagnosis:** We develop a multimodal UAM framework that effectively integrates cell radiomics with corresponding image data. Experiments demonstrate state-of-the-art results on cell classification and image segmentation tasks, achieving 92% cell classification accuracy and 72.06 mIoU.

2. Related Work

2.1. Radiomics Data Analysis

In the medical domain, radiomics data comprise a variety of quantitative descriptors, including *shape features* (e.g.,

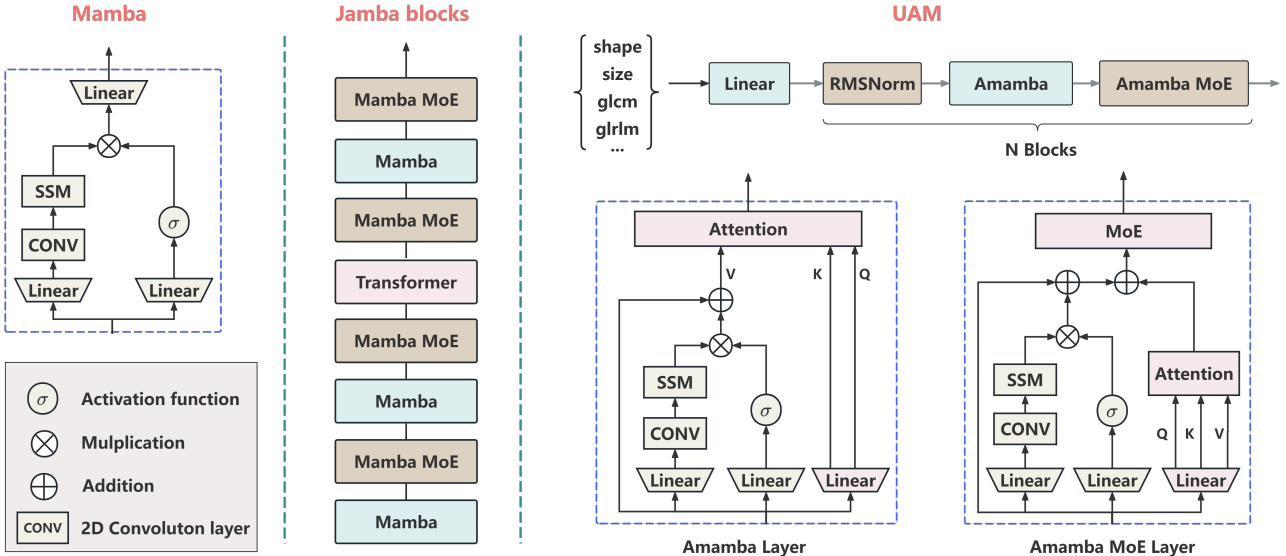


Figure 2. Overall architecture of the proposed Unified Attention-Mamba (UAM) block. Unlike Jamba, UAM integrates normalization, Amamba, and Amamba-MoE layers without fixed ratio constraints, enabling flexible fusion of attention and Mamba mechanisms. Specifically, the Amamba layer leverages Mamba to generate cross-attention values, efficiently enhancing long-range dependency modeling. Meanwhile, the Amamba-MoE layer concatenates Mamba and self-attention outputs within a mixture-of-experts (MoE) framework, providing a comprehensive, multi-perspective representation of radiomics information for advanced processing.

diameters), *first-order statistical features* (e.g., voxel intensity distributions), *second-order statistical features* (e.g., gray-level co-occurrence matrices), and *higher-order statistical features* [22, 25, 36]. Existing studies have primarily focused on patch-level and slide-level radiomics features extracted from image patches or whole-slide images [9, 13, 38]. For example, Lou *et al.* [21] enhanced MRI analysis by introducing a *radiomics error*, a reconstruction loss between ground-truth and model-generated radiomics features, thereby improving the quality of image encoders for medical understanding. Similarly, Tian *et al.* [31] employed the Swin Transformer [19] to encode image features into embeddings fused with radiomics features, increasing tumor prediction AUC from 71% to 75%.

However, these studies overlook fine-grained cell radiomics data, which are critical for detailed tumor cell characterization. Recently, ClinSegAI [3] introduces a post-processing framework built upon BiomedParse [39], a large-scale medical image foundation model trained on millions of image–mask–text triples [40]. ClinSegAI improves slide-level segmentation through multi-patch-guided refinement and establishes a framework for generating cell radiomics features for medical analysis. Nevertheless, it does not exploit these cell radiomics for predictive modeling.

2.2. Hybrid Architectures

While the Transformer architecture has long dominated both vision and language domains [1, 24], the Mamba

model, built upon the State Space Model (SSM) [6, 7], has recently emerged as a powerful alternative. Mamba offers linear computational complexity and excels at capturing long-range dependencies, making it increasingly attractive for large-scale sequence modeling. Recent research has extended Mamba and SSM variants to diverse domains, including GSS [23], Vision Mamba [42], and VM-Unet [26]. To combine the strengths of both paradigms, hybrid Attention–Mamba structures have gained growing interest. Jamba [15, 30] is among the first to explore this integration, identifying an optimal ratio between Transformer and Mamba layers. However, its fixed-layer ratio constrains architectural flexibility and limits generalization. MFuser [35] introduces an enhancer block to integrate Vision Foundation Models and Vision–Language Models. BMTNet [41] and Tamba [10] design hybrid strategies for demosaicing and forecasting tasks. Nevertheless, none of these architectures serves as a unified foundational backbone for understanding a single modality. In contrast, our proposed UAM represents the first Unified Attention–Mamba architecture specifically designed for cell radiomics data, offering a flexible and efficient backbone tailored to sequence-like radiomics features.

3. Methods

In this section, we first formulate the cell radiomics classification problem. We then present a detailed description of

our proposed Unified Attention-Mamba model, highlighting its two key components, the Amamba and Amamba-MoE encoders. Finally, we describe the multimodal extension of UAM, which integrates radiomics and image features for joint tumor cell classification and segmentation.

3.1. Problem Formulation

In the radiomics field, given the source medical images (i.e., H&E images) $X^m = \{x_i^m\}_{i=1}^N$, where $x_i^m \in \mathbb{R}^{H \times W \times 3}$, N denotes the number of medical images, PyRadiomics [32] can generate the corresponding slide-level radiomics features $X^r = \{x_i^r\}_{i=1}^N$ based on X^m , where $x_i^r \in \mathbb{R}^{1 \times F \times D}$, F represents the number of radiomics features, and D denotes the feature dimensions. As we adopt the advanced post-processing framework of ClinsegAI [3], it can generate the cell masks $Y^c = \{y_i^c\}_{i=1}^N$ and cell class labels $Y^s = \{y_i^s\}_{i=1}^N$. We can then obtain the cell radiomics $X^c = \{x_i^c\}_{i=1}^N$ based on both images X^m and cell masks Y^c , where $x_i^c \in \mathbb{R}^{L \times F \times D}$, L represents the number of cells in each image. More details about the generation of cell radiomics data can be found in Section 4.

A radiomics classification model needs to analyze the cell radiomics X^c and predict the cell labels $Y^p = \{y_i^p\}_{i=1}^N$. Due to the long sequence and well-defined values of the radiomics features, x_i^c can be expressed as $x_i^c = \{x_{it}^c\}_{t=1}^l$, where we reshape the radiomics features of one cell into several sequences l . A linear layer is initially employed for processing input x_{it}^c ,

$$x_{it}^f = \text{Linear}(x_{it}^c), \quad (1)$$

where $\text{Linear}(\cdot)$ is the linear projection. Moreover, following the Jamba [15], we also add the RMSNorm [34] at the beginning of each block, which can be expressed as:

$$\bar{x}_{it}^f = \text{RMSNorm}(x_{it}^f). \quad (2)$$

Further, the \bar{x}_{it}^f is forwarded to the Amamba and Amamba-MoE layer, which can be defined as:

$$\bar{x}_{it}^a = A^m(\bar{x}_{it}^f), \quad (3)$$

where $A(\cdot)$ denotes the function of Amamba, and $A^m(\cdot)$ denotes the Amamba-MoE layer. They are the backbone of radiomics understanding and analysis, as shown in Figure 2.

Next, we will delve into the details of the Amamba and Amamba-MoE, along with the multimodal architecture.

3.2. Amamba Encoder

Given the high-throughput nature of radiomics data, it is crucial to identify effective methods for extracting feature dependency information and generating comprehensive global representations. This paper presents a novel and practical backbone for encoding radiomics features, designed to effectively capture long-range dependency information, thereby facilitating cross-attention mechanisms to

focus on important radiomics features and generate embeddings with more meaningful global information. Given that Mamba [6] enables efficient extraction of long-range dependencies in linear time, we employ the SSM to encode features as the values V_{it} in the cross-attention module, while using the original input embeddings as the query Q_i and key K_i . Thus, \bar{x}_i^f will first be computed as:

$$\begin{aligned} g_{it} &= \sigma(\text{Linear}(\bar{x}_{it}^f)), \\ h_{it} &= (1 - g_{it})h_{i(t-1)} + g_{it}\bar{x}_{it}^f. \end{aligned} \quad (4)$$

where $h_{i(t-1)}$ is the hidden state at the t th sequence derived from state space model (SSM) [6]. h_{it} will then be embedded into cross-attention, which is defined as:

$$\bar{V}_{it} = W_v^T(h_{it} + \bar{x}_{it}^f), \quad K_{it} = W_k^T\bar{x}_{it}^f, \quad Q_{it} = W_q^T\bar{x}_{it}^f, \quad (5)$$

where we add one residual connection for h_{it} to enhance the stability of modules, similar to the Jamba [15]. Thus, the final outputs of Amamba should be:

$$O_{it}^a = \text{softmax}\left(\frac{Q_{it}K_{it}^T}{\sqrt{d_k}}\right)\bar{V}_{it}, \quad (6)$$

where d_k denotes the dimensionality of the key vectors. With Amamba, UAM can encode radiomics features into an embedding that includes richer global information.

3.3. Amamba-MoE Encoder

Mixture of Experts (MoE) [11, 27] has gained increasing attention in both the vision and language fields, as it enables sparsely activated models with multiple expert networks while maintaining low computation costs. In this work, we incorporate the MoE mechanism into the proposed AMamba-MoE encoder. Unlike existing transformer-MoE or Mamba-MoE architectures [5, 15], our design integrates the outputs of self-attention and Mamba modules as inputs to the MoE layer, thereby enhancing model performance through hybrid structural synergy. This integration allows the model to leverage global information from multiple perspectives, enabling each expert to process richer and more diverse feature representations. Specifically, the integrated embeddings are computed by:

$$O_{it}' = \text{Concatenate}(\text{self-atten}(O_{it}^a), \text{Mamba}(O_{it}^a)), \quad (7)$$

where $\text{self-atten}(\cdot)$ represents the self-attention. The MoE then processed the integrated embeddings as:

$$O_{it}^{am} = \text{MoE}(O_{it}' + O_{it}^a), \quad (8)$$

where O_{it}^{am} denotes the final outputs of Amamba-MoE. Analogous to the Amamba encoder, the Amamba-MoE module incorporates a residual connection. This design aims to unify the strengths of heterogeneous architectures within a streamlined structure, thereby improving the model's representational and learning capabilities.

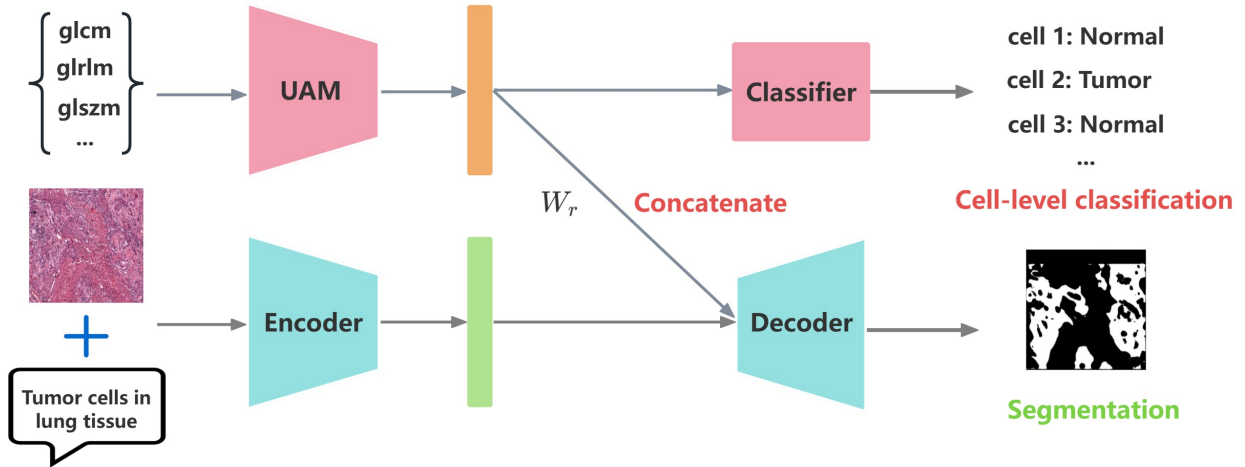


Figure 3. Overview of the multimodal model architecture. The proposed model leverages radiomics data for tumor cell classification and integrates cell radiomics, image, and prompt information for effective tumor segmentation. Cell radiomics embeddings are projected into the image embedding space to enable seamless multimodal fusion. A pretrained BiomedParse encoder is employed for joint image–text feature extraction, while its decoder generates segmentation masks based on the concatenated multimodal embeddings.

Remark 1 *The Amamba encoder is designed to capture enhanced global information within a unified hybrid architecture for generating radiomic embeddings. In contrast, the Amamba-MoE encoder emphasizes leveraging the fused Mamba and Attention outputs to facilitate MoE processing and model capability. Crucially, both encoders benefit from the inherent strengths of the Mamba and attention mechanisms, allowing the model to encode more effectively.*

Therefore, the UAM backbone leverages the Amamba and the Amamba-MoE layers to encode cell radiomics data, facilitating cell classification. For simplicity, yet without loss of generality, the UAM is optimized by cross-entropy loss.

3.4. Multimoal Framework

Inspired by the success of BiomedParse [39] in medical image segmentation, we propose a multimodal framework that integrates the proposed UAM into BiomedParse, which enables the utilization of leveraging both cell radiomics, images, and prompt text for model learning, as shown in Figure 3. Following the work of LLAVA [17, 18], the embeddings of radiomics features will be projected into the dimensions of the image and prompt, which are expressed as:

$$z_i^r = \text{MLP}(e_i^r), \quad (9)$$

where $\text{MLP}(\cdot)$ is a projection function, e^r denotes the radiomics embeddings from UAM. We then concatenate two embeddings as follows:

$$z_i^c = \text{Concatenate}(z_i^r, z_i^m), \quad (10)$$

where z_i^m are the corresponding embeddings of image and prompt from the BiomedParse encoder. z_i^c then can be leveraged for the BiomedParse decoder to generate tumor region mask [39]

$$\text{mask}_i = \text{Decoder}(z_i^c). \quad (11)$$

Within this framework, cell radiomics provides granular information about tumor cells, enhancing the representation and understanding of tumor regions, thereby enabling the model to achieve better segmentation performance. Furthermore, the proposed multimodal framework enables the utilization of cell radiomics features to identify cell-level labels, thereby expanding the applicability of BiomedParse [39] and ClinSegAI [3]. Consequently, this multimodal framework enhances the accuracy of fine-grained clinical diagnosis and supports more precise treatment planning. During the training stage, we utilize the original loss of BiomedParse [39] plus the classification loss to optimize the whole model.

4. Experiments

In this section, we first describe the experimental settings and implementation details. Next, we present the results of the proposed UAM and its multimodal extension, comparing them against several baseline methods. Finally, we provide visualizations of cell classification results of UAM.

4.1. Experiment Settings

Datasets. We evaluated our model based on three cancer datasets, including WSSS4LUAD [8], IGNITE [28], and

Table 1. Tumor cell classification results in comparison with baselines on four cell radiomics datasets. *Combined*: WSSS4LUAD + IGNITE; *+TCGA*: WSSS4LUAD + IGNITE + TCGA. **Green** highlights: UAM variants. **Bold**: best performance.

Datasets	Metric	Trans [33]	Trans-M [5]	Mamba [6]	Mamba-M [15]	Jamba [15]	UAM-L	UAM-M	UAM
WSSS4LUAD	Accuracy	85.77%	86.52%	90.65%	89.35%	88.96%	91.71%	90.41%	92.06%
	F1	81.53%	81.71%	88.27%	87.02%	85.31%	88.72%	87.90%	89.70%
	AUC	91.81%	91.73%	94.60%	95.67%	94.63%	93.40%	93.80%	95.90%
IGNITE	Accuracy	77.56%	77.83%	77.95%	77.94%	78.05%	77.97%	77.87%	78.53%
	F1	76.88%	76.89%	77.49%	77.46%	77.23%	77.55%	77.59%	77.73%
	AUC	86.13%	86.40%	86.60%	86.52%	86.12%	86.62%	86.55%	86.71%
Combined	Accuracy	78.71%	78.64%	78.40%	79.50%	79.45%	79.55%	79.39%	80.70%
	F1	77.11%	76.97%	76.99%	77.94%	77.69%	77.96%	78.28%	79.34%
	AUC	87.05%	87.13%	86.82%	87.64%	87.80%	87.87%	87.91%	88.80%
+TCGA	Accuracy	82.27%	82.70%	83.01%	83.33%	78.61%	84.20%	84.24%	84.33%
	F1	79.70%	79.79%	80.57%	80.57%	71.69%	81.48%	81.53%	81.45%
	AUC	90.37%	90.50%	91.18%	91.15%	75.60%	91.79%	91.94%	91.91%

Table 2. Cross-validation results for tumor cell classification with competitive baselines. Models are trained on the IGNITE dataset and tested on other datasets. *+TCGA*: WSSS4LUAD + TCGA. **Green** highlights: UAM variants. **Bold**: best performance.

Datasets	Metric	Trans [33]	Trans-M [5]	Mamba [6]	Mamba-M [15]	Jamba [15]	UAM-L	UAM-M	UAM
WSSS4LUAD	Accuracy	77.54%	79.70%	77.58%	78.45%	76.62%	78.96%	79.27%	81.76%
	F1	73.45%	73.42%	70.26%	71.65%	70.21%	73.49%	72.36%	74.84%
	AUC	83.56%	83.48%	76.14%	82.13%	80.63%	84.75%	83.80%	84.46%
+TCGA	Accuracy	80.65%	77.29%	66.48%	64.65%	56.37%	88.22%	72.27%	86.57%
	F1	80.13%	65.73%	62.55%	65.36%	50.68%	82.38%	70.25%	81.06%
	AUC	91.45%	73.51%	64.34%	68.62%	57.63%	96.13%	66.80%	98.54%

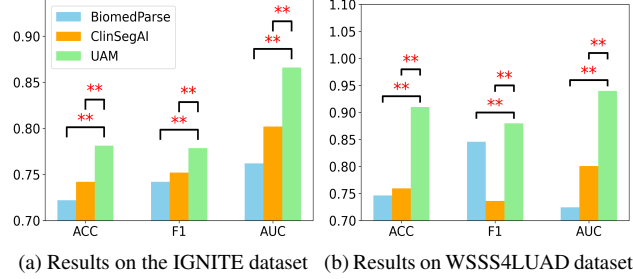


Figure 4. Comparison with the image-based SOTA models for cell classification on the IGNITE dataset and WSSS4LUAD dataset. **: p-value < 0.01 (two sample t-tests).

TCGA [2]. The WSSS4LUAD dataset includes 309 H&E patches and corresponding annotated masks (i.e., tumor or non-tumor), with a resolution of 1024×1024 . The IGNITE dataset includes 406 H&E patches with the same resolutions, and its annotations are generated from both machine and experts. The TCGA dataset contains 848 selected H&E normal tissue patches to balance the distribution of class labels in WSSSLUAD and IGNITE datasets. For the cell classification task, cell radiomics data need to be gen-

erated from the corresponding image datasets. As shown in Section 1 and Figure 1, the cell-level radiomic features were extracted from H&E images using the cell masks generated by ClinSegAI [3], with the PyRadiomics package (v3.1.0) [32] in Python. The extracted features encompassed shape-based metrics, first-order intensity statistics, and texture descriptors. More details about data preparation can be found in our *Supplemental Material*. Specifically, the WSSS4LUAD dataset contained 153,702 cells, the IGNITE dataset included 349,882 cells, and the TCGA dataset comprised 112,001 cells. Except for cross-validation, we divided the four datasets into training and testing sets using an 8:2 ratio, ensuring the split is performed based on distinct individuals.

Implementation Details. During training, the number of UAM blocks and other baseline modules was set to 4, with additional details provided in the ablation studies. The batch size was 64 for the cell radiomics data and 4 for the multimodal framework. The AdamW optimizer [20] was employed with a learning rate 1×10^{-4} . All experiments were conducted on a single NVIDIA RTX A6000 GPU with 49 GB of memory.

Table 3. Comparative image segmentation results between the proposed multimodal model and BiomedParse. *Combined+TCGA*: WSSS4LUAD + IGNITE + TCGA. **Bold**: best performance. Symbol \uparrow : higher values are preferred.

Datasets	Methods	Precision \uparrow	cIoU \uparrow	mIoU \uparrow	cDICE \uparrow	mDICE \uparrow
WSSS4LUAD	BiomedParse	88.04	80.16	73.48	88.98	83.52
	UAM	90.21	80.64	73.69	89.28	83.45
IGNITE	BiomedParse	75.34	74.13	63.47	85.14	73.51
	UAM	80.82	74.94	66.71	85.67	76.83
Combined+TCGA	BiomedParse	88.54	76.95	70.86	86.97	81.05
	UAM	90.45	78.11	72.06	87.71	81.85

Table 4. Efficiency comparison with competitive baselines. Symbol \downarrow : lower values are preferred.

Methods	Flops (K) \downarrow	Parameters (K) \downarrow
Trans [33]	384.26	6.642
Mamba [6]	305.41	5.546
Jamba [15]	470.02	15.858
UAM-L	436.48	7.722
UAM-M	379.14	6.770
UAM	407.81	13.554

4.2. Comparison with State-of-The-Art Methods

Tumor Cell Classification. We first evaluated the model performance on the cell classification task using only cell radiomics data. Since most vision and language models are not capable of handling this setting, we replaced the main block of the UAM with several state-of-the-art (SOTA) architectures for comparison, including Transformer [33] (abbreviated as Trans), Transformer-MoE [5] (abbreviated as Trans-M), Mamba [6], Mamba-MoE [15] (proposed in Jamba and abbreviated as Mamba-M), and Jamba [15]. In addition, we introduced two ablated variants of UAM in comparison: UAM-L, which includes only the Amamba encoder, and UAM-M, which contains only the Amamba-MoE encoder. These variants serve as an ablation study of the UAM architecture, further discussed in Section 4.3.

As shown in Table 1, our proposed methods consistently outperform all baselines across three metrics, accuracy, F1 score, and AUC. Specifically, UAM achieves 92.06% accuracy on the WSSS4LUAD dataset, surpassing Mamba (90.65%), Mamba-M (89.35%), Jamba (88.96%), and Transformer (85.77%). Moreover, both UAM variants outperform competing methods on the IGNITE dataset as well as on the combined dataset. These results demonstrate that UAM effectively enhances global information extraction through its unified architecture, validating the efficacy of the proposed approach.

Furthermore, we evaluated the generalization ability of UAM in comparison with several SOTA baselines, as

shown in Table 2. Specifically, each model was trained on the IGNITE dataset, which contains the largest number of cell radiomics samples, and subsequently tested on the WSSS4LUAD dataset as well as on the combined WSSS4LUAD-TCGA dataset. UAM consistently outperforms all competing baselines, demonstrating its superior capability in learning universal radiomics representations.

Notably, Jamba exhibited severe generalization deficiencies when applied to radiomics data using the same number of blocks as other baselines. This observation suggests that its rigid hybrid design, which enforces a fixed ratio between Transformer and Mamba components, is suboptimal for cell radiomics analysis and prone to overfitting.

Comparisons with Imaged-based SOTA. We also compared UAM with two image-based SOTA methods, including BiomedParse [39] and ClinSegAI [3]. As shown in Figure 4, UAM achieves significantly higher accuracy than both BiomedParse and ClinSegAI ($p < 0.01$, two-sample t-tests) on the IGNITE and WSSS4LUAD datasets. These results demonstrate that our cell radiomics-based model effectively exploits richer cellular feature information and surpasses image-based approaches, thereby improving diagnostic accuracy. More details about their cell classification process are illustrated in the *Supplemental Material*.

Tumor Segmentation. We further evaluated the proposed multimodal UAM framework on the image segmentation task. The Precision, cIoU, mIoU, cDICE, and mDICE metrics are used to evaluate the segmentation performance. For more evaluation details, please refer to the *Supplemental Material*. As shown in Table 3, integrating UAM notably enhances the segmentation performance of BiomedParse. Specifically, the multimodal model improves the precision from 75.34 to 80.02 on the IGNITE dataset, and increases mIoU from 70.86 to 72.06 on the combined dataset. These results highlight the effectiveness of radiomics embeddings generated by UAM and demonstrate that incorporating fine-grained cell radiomics information substantially improves tumor segmentation. This underscores the broad applicability of UAM for enhancing multimodal medical analysis.

Efficiency. We evaluated the computational efficiency

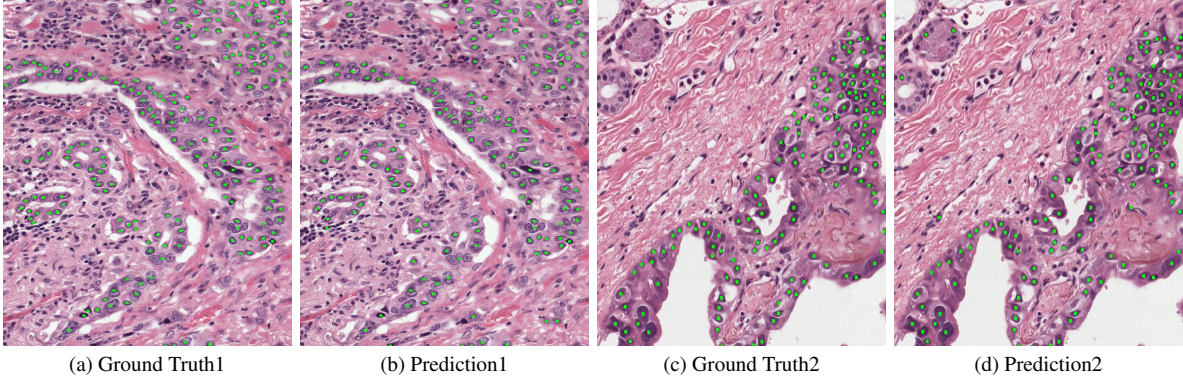


Figure 5. Visual comparison of ground truth and UAM predictions on the IGNITE dataset. Tumor cells are highlighted in green.

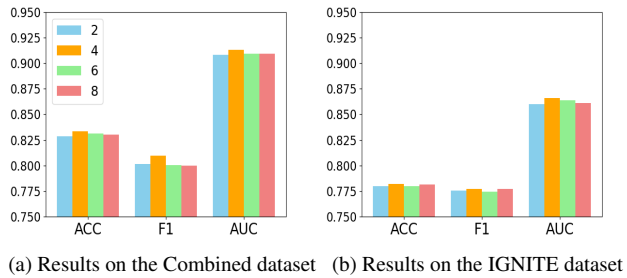


Figure 6. Ablation studies evaluating the impact of varying the number of UAM blocks on the IGNITE dataset and the combined dataset (WSSS4LUAD + IGNITE).

of UAM by measuring its Flops and total number of parameters in comparison with SOTA models, as shown in Table 4. As a unified Attention-Mamba structure, UAM naturally exhibits higher FLOPs and parameter counts than models based solely on Transformers or Mamba. However, it achieves significantly lower FLOPs and parameter complexity than Jamba, demonstrating UAM’s superior efficiency and flexibility resulting from its unified design. Notably, UAM-M achieves even lower FLOPs than Transformer, indicating that the Amamba-MoE encoder enables faster processing through its streamlined hybrid structure.

Visualization and AI Interpretability. As illustrated in Figure 5, UAM effectively highlights tumor cells on H&E slides based on radiomics data, facilitating pathologist interpretation and enhancing AI explainability.

4.3. Ablation Study

We conducted ablation experiments with two model variants, UAM-L and UAM-M, to systematically evaluate the contributions of different components. As shown in Table 1, UAM-M achieves the best overall performance when all datasets are combined, demonstrating the effectiveness of the Amamba-MoE encoder. This confirms our hypothe-

sis that the Mixture-of-Experts (MoE) mechanism enhances the radiomics representation capability of hybrid architectures, particularly on large-scale datasets. Furthermore, Table 2 shows that UAM-L exhibits comparable generalization performance to the full UAM model, indicating that the Amamba encoder effectively captures universal radiomics representations. Nevertheless, UAM consistently outperforms both ablated variants across most evaluation scenarios, underscoring the complementary advantages of combining the Amamba and Amamba-MoE encoders.

In addition, we varied the number of UAM blocks to assess the impact of this hyperparameter (set to Block = 4 in our final configuration). As illustrated in Figure 6, increasing the number of blocks leads to overfitting due to the low dimensionality of cell radiomics features, whereas reducing the block number to two causes a performance drop.

5. Conclusion

In this work, we presented UAM, the first dedicated backbone for cell radiomics analysis and tumor classification. UAM unifies the strengths of the Transformer and Mamba architectures within a single framework, eliminating the need for ratio tuning and substantially enhancing radiomics representation learning. It comprises two core components: the Amamba encoder, which leverages Mamba-generated embeddings within a cross-attention mechanism to capture global dependencies, and the Amamba-MoE encoder, which integrates a Mixture-of-Experts module to efficiently process fused attention-Mamba outputs and improve model capacity. Moreover, we introduced a multimodal UAM framework that integrates image and cell radiomics features for joint tumor classification and segmentation. Extensive experiments demonstrate that UAM achieves state-of-the-art performance across multiple datasets and tasks, validating its effectiveness, flexibility, and generalization ability. These results highlight the potential of UAM as a foundation for radiomics-driven cancer diagnosis and the integration

tive analysis of multimodal biomedical data.

References

- [1] Josh Achiam, Steven Adler, Sandhini Agarwal, Lama Ahmad, Ilge Akkaya, Florencia Leoni Aleman, Diogo Almeida, Janko Altenschmidt, Sam Altman, Shyamal Anadkat, et al. Gpt-4 technical report. *arXiv preprint arXiv:2303.08774*, 2023.
- [2] Brad Albertina, Mark Watson, Chandra Holback, Rose Jarosz, Shanah Kirk, Yueh Lee, Kimberly Rieger-Christ, and John Lemmerman. The cancer genome atlas lung adenocarcinoma collection (tcga-luad). *The Cancer Imaging Archive*, 2016.
- [3] P. Bhajaj, S. Nalubolu, B. Gurram, M. Srinivas, R. Choudhary, W. Dai, L. Wang, T. Jamaspishvili, Z. Ding, and N. L. Guo. Clinsegai: A post-processing framework for superior histopathology segmentation accuracy, radiomics feature preservation, and quantitative analysis. *Computers in Biology and Medicine*, 2025.
- [4] Alexey Dosovitskiy, Lucas Beyer, Alexander Kolesnikov, Dirk Weissenborn, Xiaohua Zhai, Thomas Unterthiner, Mostafa Dehghani, Matthias Minderer, Georg Heigold, Sylvain Gelly, Jakob Uszkoreit, and Neil Houlsby. An image is worth 16x16 words: Transformers for image recognition at scale. In *Proceedings of the International Conference on Learning Representations*, 2021.
- [5] William Fedus, Barret Zoph, and Noam Shazeer. Switch transformers: Scaling to trillion parameter models with simple and efficient sparsity. *Journal of Machine Learning Research*, 23(120):1–39, 2022.
- [6] Albert Gu and Tri Dao. Mamba: Linear-time sequence modeling with selective state spaces. In *Proceedings of the First Conference on Language Modeling*, 2024.
- [7] Albert Gu, Karan Goel, and Christopher Ré. Efficiently modeling long sequences with structured state spaces. *arXiv preprint arXiv:2111.00396*, 2021.
- [8] Chu Han, Xipeng Pan, Lixu Yan, Huan Lin, Bingbing Li, Su Yao, Shanshan Lv, Zhenwei Shi, Jinhai Mai, Jiatai Lin, et al. Wsss4luad: Grand challenge on weakly-supervised tissue semantic segmentation for lung adenocarcinoma. *arXiv preprint arXiv:2204.06455*, 2022.
- [9] Lili Huang, Zhuoyuan Li, Xiaolei Zhu, Hui Zhao, Chenglu Mao, Zhihong Ke, Yuting Mo, Dan Yang, Yue Cheng, Ruomeng Qin, et al. Deep adaptive learning predicts and diagnoses cvsd-related cognitive decline using radiomics from t2-flair: a multi-centre study. *NPJ Digital Medicine*, 8(1):444, 2025.
- [10] Yizhou Huang, Yihua Cheng, and Kezhi Wang. Trajectory mamba: Efficient attention-mamba forecasting model based on selective ssm. In *Proceedings of the Computer Vision and Pattern Recognition Conference*, pages 12058–12067, 2025.
- [11] Albert Q Jiang, Alexandre Sablayrolles, Antoine Roux, Arthur Mensch, Blanche Savary, Chris Bamford, Devendra Singh Chaplot, Diego de las Casas, Emma Bou Hanna, Florian Bressand, et al. Mixtral of experts. *arXiv preprint arXiv:2401.04088*, 2024.
- [12] Virendra Kumar, Yuhua Gu, Satrajit Basu, Anders Berglund, Steven A Eschrich, Matthew B Schabath, Kenneth Forster, Hugo JW Aerts, Andre Dekker, David Fenstermacher, et al. Radiomics: the process and the challenges. *Magnetic resonance imaging*, 30(9):1234–1248, 2012.
- [13] Jiangwei Lao, Yinseng Chen, Zhi-Cheng Li, Qihua Li, Ji Zhang, Jing Liu, and Guangtao Zhai. A deep learning-based radiomics model for prediction of survival in glioblastoma multiforme. *Scientific reports*, 7(1):10353, 2017.
- [14] Hao Li, Han Liu, Heinrich von Busch, Robert Grimm, Henk-jan Huisman, Angela Tong, David Winkel, Tobias Penzkofer, Ivan Shabunin, Moon Hyung Choi, et al. Deep learning-based unsupervised domain adaptation via a unified model for prostate lesion detection using multisite biparametric mri datasets. *Radiology: Artificial Intelligence*, 6(5):e230521, 2024.
- [15] Opher Lieber, Barak Lenz, Hofit Bata, Gal Cohen, Jhonathan Osin, Itay Dalmedigos, Erez Safahi, Shaked Meiron, Yonatan Belinkov, Shai Shalev-Shwartz, et al. Jamba: A hybrid transformer-mamba language model. *arXiv preprint arXiv:2403.19887*, 2024.
- [16] Elaine Johanna Limkin, Roger Sun, Laurent Dercle, Evangelia I Zacharaki, Charlotte Robert, Sylvain Reuzé, Antoine Schernberg, Nikos Paragios, Eric Deutsch, and Charles Ferté. Promises and challenges for the implementation of computational medical imaging (radiomics) in oncology. *Annals of Oncology*, 28(6):1191–1206, 2017.
- [17] Haotian Liu, Chunyuan Li, Qingyang Wu, and Yong Jae Lee. Visual instruction tuning. In *Proceedings of the Advances in Neural Information Processing Systems*, pages 34892–34916, 2023.
- [18] Haotian Liu, Chunyuan Li, Yuheng Li, and Yong Jae Lee. Improved baselines with visual instruction tuning. In *Proceedings of the IEEE/CVF conference on computer vision and pattern recognition*, pages 26296–26306, 2024.
- [19] Ze Liu, Yutong Lin, Yue Cao, Han Hu, Yixuan Wei, Zheng Zhang, Stephen Lin, and Baining Guo. Swin transformer: Hierarchical vision transformer using shifted windows. In *Proceedings of the IEEE/CVF international conference on computer vision*, pages 10012–10022, 2021.
- [20] Ilya Loshchilov and Frank Hutter. Decoupled weight decay regularization. In *Proceedings of the International Conference on Learning Representations*, 2019.
- [21] Bin Lou, Semihcan Doken, Tingliang Zhuang, Danielle Wingerter, Mishka Gidwani, Nilesh Mistry, Lance Ladic, Ali Kamen, and Mohamed E Abazeed. An image-based deep learning framework for individualising radiotherapy dose: a retrospective analysis of outcome prediction. *The Lancet Digital Health*, 1(3):e136–e147, 2019.
- [22] Marius E Mayerhoefer, Andrzej Materka, Georg Langs, Ida Häggström, Piotr Szczypinski, Peter Gibbs, and Gary Cook. Introduction to radiomics. *Journal of Nuclear Medicine*, 61(4):488–495, 2020.
- [23] Harsh Mehta, Ankit Gupta, Ashok Cutkosky, and Behnam Neyshabur. Long range language modeling via gated state spaces. *arXiv preprint arXiv:2206.13947*, 2022.
- [24] William Peebles and Saining Xie. Scalable diffusion models with transformers. In *Proceedings of the IEEE/CVF international conference on computer vision*, pages 10012–10022, 2021.

national conference on computer vision, pages 4195–4205, 2023.

[25] Stefania Rizzo, Francesca Botta, Sara Raimondi, Daniela Origgi, Cristiana Fanciullo, Alessio Giuseppe Morganti, and Massimo Bellomi. Radiomics: the facts and the challenges of image analysis. *European radiology experimental*, 2(1):36, 2018.

[26] Jiacheng Ruan, Jincheng Li, and Suncheng Xiang. Vm-unet: Vision mamba unet for medical image segmentation. *ACM Transactions on Multimedia Computing, Communications and Applications*, 2024.

[27] Noam Shazeer, Azalia Mirhoseini, Krzysztof Maziarz, Andy Davis, Quoc Le, Geoffrey Hinton, and Jeff Dean. Outrageously large neural networks: The sparsely-gated mixture-of-experts layer. *arXiv preprint arXiv:1701.06538*, 2017.

[28] Joey Spronck, Leander van Eekelen, Dominique van Midden, Joep Bogaerts, Leslie Tessier, Valerie Dechering, Mu-radije Demirel-Andishmand, Gabriel Silva de Souza, Roland Nemeth, Enrico Munari, et al. A tissue and cell-level annotated h&e and pd-l1 histopathology image dataset in non-small cell lung cancer. *arXiv preprint arXiv:2507.16855*, 2025.

[29] Martijn PA Starmans, Sebastian R van der Voort, Jose M Castillo Tovar, Jifke F Veenland, Stefan Klein, and Wiro J Niessen. Radiomics: data mining using quantitative medical image features. In *Handbook of medical image computing and computer assisted intervention*, pages 429–456. Elsevier, 2020.

[30] Jamba Team, Barak Lenz, Alan Arazi, Amir Bergman, Avshalom Manevich, Barak Peleg, Ben Aviram, Chen Almagor, Clara Fridman, Dan Padnos, et al. Jamba-1.5: Hybrid transformer-mamba models at scale. *arXiv preprint arXiv:2408.12570*, 2024.

[31] Weiwei Tian, Qinjin Yan, Xinyu Huang, Rui Feng, Fei Shan, Daoying Geng, and Zhiyong Zhang. Predicting occult lymph node metastasis in solid-predominantly invasive lung adenocarcinoma across multiple centers using radiomics-deep learning fusion model. *Cancer Imaging*, 24(1):8, 2024.

[32] Joost JM Van Griethuysen, Andriy Fedorov, Chintan Parmar, Ahmed Hosny, Nicole Aucoin, Vivek Narayan, Regina GH Beets-Tan, Jean-Christophe Fillion-Robin, Steve Pieper, and Hugo JW Aerts. Computational radiomics system to decode the radiographic phenotype. *Cancer research*, 77(21):e104–e107, 2017.

[33] Ashish Vaswani, Noam Shazeer, Niki Parmar, Jakob Uszkoreit, Llion Jones, Aidan N Gomez, Łukasz Kaiser, and Illia Polosukhin. Attention is all you need. In *Proceedings of the Advances in neural information processing systems*, 2017.

[34] Biao Zhang and Rico Sennrich. Root mean square layer normalization. In *Proceedings of the Advances in Neural Information Processing Systems*, 2019.

[35] Xin Zhang and Robby T Tan. Mamba as a bridge: Where vision foundation models meet vision language models for domain-generalized semantic segmentation. In *Proceedings of the Computer Vision and Pattern Recognition Conference*, pages 14527–14537, 2025.

[36] Xingping Zhang, Yanchun Zhang, Guijuan Zhang, Xingtong Qiu, Wenjun Tan, Xiaoxia Yin, and Liefa Liao. Deep learning with radiomics for disease diagnosis and treatment: challenges and potential. *Frontiers in oncology*, 12:773840, 2022.

[37] Yun-Feng Zhang, Chuan Zhou, Sheng Guo, Chao Wang, Jin Yang, Zhi-Jun Yang, Rong Wang, Xu Zhang, and Feng-Hai Zhou. Deep learning algorithm-based multimodal mri radiomics and pathomics data improve prediction of bone metastases in primary prostate cancer. *Journal of Cancer Research and Clinical Oncology*, 150(2):78, 2024.

[38] Yun-Feng Zhang, Chuan Zhou, Sheng Guo, Chao Wang, Jin Yang, Zhi-Jun Yang, Rong Wang, Xu Zhang, and Feng-Hai Zhou. Deep learning algorithm-based multimodal mri radiomics and pathomics data improve prediction of bone metastases in primary prostate cancer. *Journal of Cancer Research and Clinical Oncology*, 150(2):78, 2024.

[39] Theodore Zhao, Yu Gu, Jianwei Yang, Naoto Usuyama, Ho Hin Lee, Tristan Naumann, Jianfeng Gao, Angela Crabtree, Jacob Abel, Christine Moung-Wen, et al. Biomed-parse: a biomedical foundation model for image parsing of everything everywhere all at once. *arXiv preprint arXiv:2405.12971*, 2024.

[40] Theodore Zhao, Yu Gu, Jianwei Yang, Naoto Usuyama, Ho Hin Lee, Sid Kiblawi, Tristan Naumann, Jianfeng Gao, Angela Crabtree, Jacob Abel, et al. A foundation model for joint segmentation, detection and recognition of biomedical objects across nine modalities. *Nature methods*, 22(1):166–176, 2025.

[41] Shiyang Zhou, Haijin Zeng, Yunfan Lu, Tong Shao, Ke Tang, Yongyong Chen, Jie Liu, and Jingyong Su. Binarized mamba-transformer for lightweight quad bayer hybridevs demosaicing. In *Proceedings of the Computer Vision and Pattern Recognition Conference*, pages 8817–8827, 2025.

[42] Lianghui Zhu, Bencheng Liao, Qian Zhang, Xinlong Wang, Wenyu Liu, and Xinggang Wang. Vision mamba: Efficient visual representation learning with bidirectional state space model. *arXiv preprint arXiv:2401.09417*, 2024.

Table 5. Statistics of three datasets.

Dataset	Total Cells	Tumor cells	Attribute	Types
WSSS	153,702	41,321	106	3
IGNITE	349,882	151,122	106	15
TCGA	112,001	0	106	1

A. Cell Radiomics Dataset Preparation

Cell-level radiomic features were extracted from H&E-stained images using cell masks generated by ClinSegAI [3]. Feature computation was performed using the PyRadiomics package (v3.1.0) in Python. The features encompassed shape-based metrics (e.g., area, perimeter), first-order intensity statistics (e.g., mean, standard deviation), and texture descriptors derived from Gray-Level Co-occurrence Matrices (GLCM) and related filters. Summary statistics for the three datasets mentioned in the article are presented in Table 5 (i.e., WSSS4LUAD dataset is abbreviated as WSSS). Specifically, the WSSS dataset [8] focuses on Lung Adenocarcinoma (LUAD) and originally categorizes cells into three distinct classes: tumor, stroma, and normal. In stark contrast, the IGNITE dataset [28] is significantly richer, encompassing fifteen different cell types (e.g., tumor, inflammatory, and liver cells) and covers a broader range of Non-Small Cell Lung Cancer (NSCLC) subtypes, including Adenocarcinoma (AD), Squamous Cell Carcinoma (SC), and Large Cell (LC). Moreover, we selected only the normal tissue slides from the TCGA cohort [2] to balance the distribution of class labels in the WSSS and IGNITE datasets.

The ground truth for each cell’s true class was established by comparing regional ground truth masks (created by human experts, containing both cellular and non-cellular areas) against the ClinSegAI cell-level masks (generated by BiomedParse [39] using the prompt ”cells”). This rigorous comparison process ensured the reliability of the cell-level ground truth labels.

B. Image-based Segmentation Model

In this study, initial tumor segmentations were generated for each slide image using BiomedParse with the prompt ”Neoplastic Cells.” Cell-level tumor prediction was subsequently derived by calculating the overlap between each cell mask and the resulting tumor segmentation. Consistent with UAM’s (Unified Attention-Mamba) configuration, a cell was classified as tumor if its tumor coverage exceeded 50%, and non-tumor otherwise.

The ClinSegAI framework, which refines BiomedParse segmentations through multi-scale post-processing algorithms [3], was also utilized for comparison. To generate

ClinSegAI-based tumor predictions, we followed the identical procedure: generating the initial tumor segmentations (BiomedParse with the prompt ”neoplastic cells”), and then applying the same 50% threshold to calculate per-cell tumor coverage for classification.

Notably, the cell-level ground truth used for evaluation (which incorporates expert input and a different ClinSegAI prompt) is distinct from the cell class predictions (tumor or non-tumor) generated solely by the ClinSegAI method.

C. Evaluation Metric

In the image segmentation task, we utilize the precision, cIoU, mIoU, cDICE, and mDICE. All metrics utilize a segmentation threshold of 0.5. Specifically, cIoU (Class IoU) represents the Intersection over Union (IoU) score calculated only for the tumor class. mIoU is the average IoU score across all n classes, which is calculated as:

$$\text{mIoU} = \frac{1}{n} \sum_i^n \text{IoU}_i \quad (12)$$

The cDICE and mDICE scores are calculated analogously: cDICE focuses solely on the tumor class segmentation performance, while mDICE computes the average DICE score across all classes.

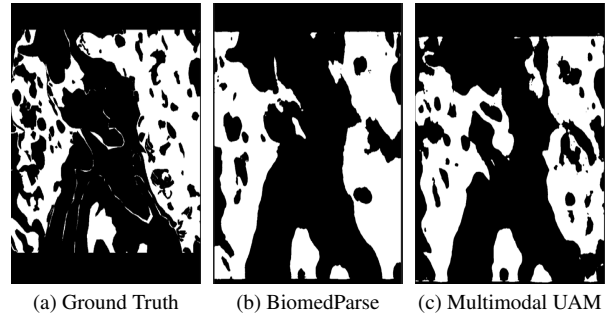


Figure 7. Visual comparison of ground truth, BiomedParse, and UAM predictions on the IGNITE dataset. The masks indicate the tumor regions.

D. More Experiment Results

We provide a visualization of the Ground Truth, BiomedParse-generated, and UAM-generated masks in Figure 7. The multimodal UAM model demonstrates the capability to provide a more accurate mask, which we attribute to its effectiveness in leveraging the cell radiomics information from each image. This finding underscores the significant advantage and effectiveness of the multimodal UAM architecture. More visualization results are shown in Figures 8, 9, 10, 11, indicating the effectiveness of UAM that highlights tumor cells on H&E slides based on radiomics data, facilitating pathologist interpretation.

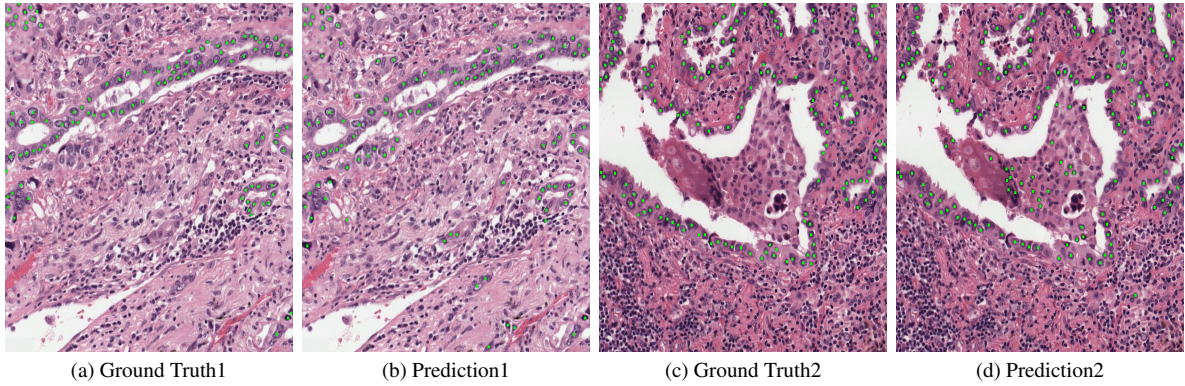


Figure 8. Visual comparison of ground truth and UAM predictions. Tumor cells are highlighted in green.

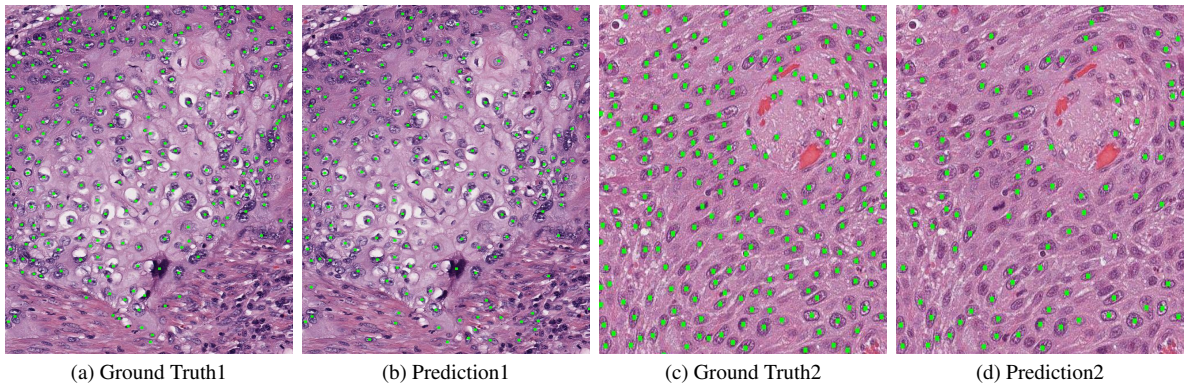


Figure 9. Visual comparison of ground truth and UAM predictions. Tumor cells are highlighted in green.

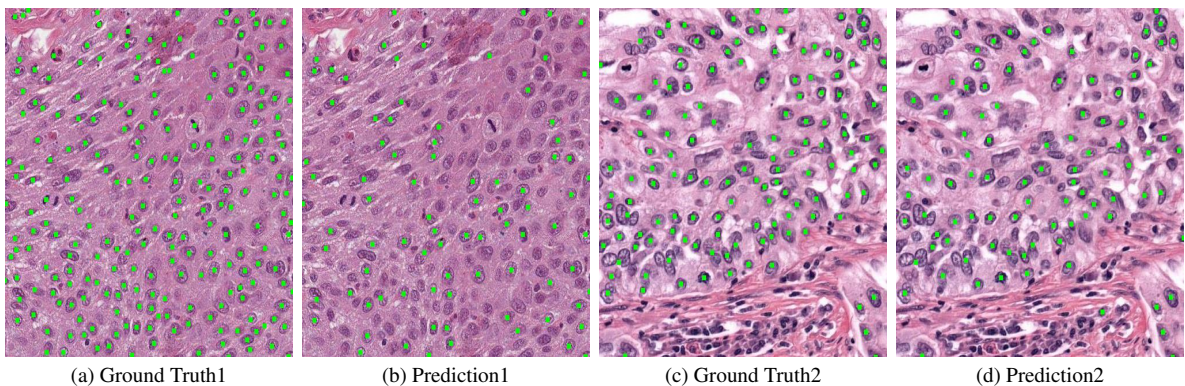


Figure 10. Visual comparison of ground truth and UAM predictions. Tumor cells are highlighted in green.

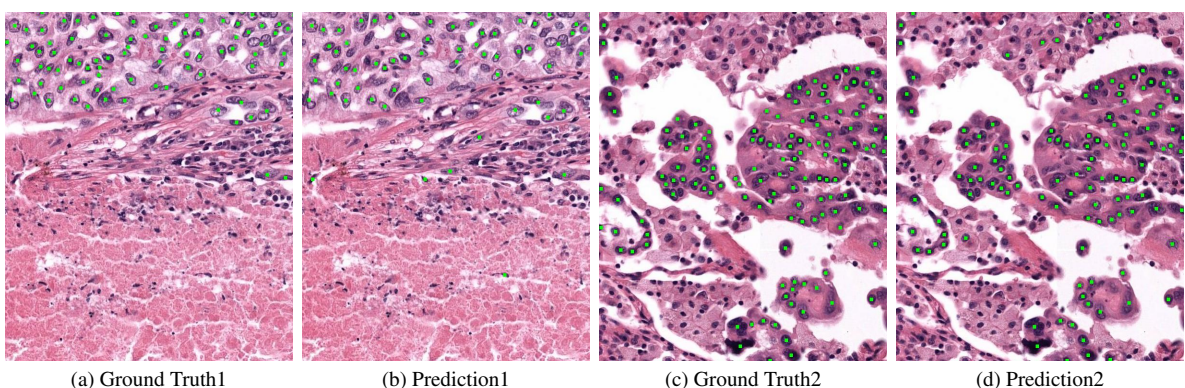


Figure 11. Visual comparison of ground truth and UAM predictions. Tumor cells are highlighted in green.